Clay Minerals (2026), **61**, 177–192
doi:10.1180/clm.2026.10034

Article

Potential use of clays from Zemlet El Beidha (southern Tunisia) as aluminosilicate precursors for geopolymer synthesis

Zainab Jrad[1], Francesco Genua[2], Isabella Lancellotti[2], Cristina Leonelli[2] and Salah Mahmoudi[1]

[1]Research Unity of Geo-systems, Geo-resources and Geo-environments (UR3G), Department of Earth Sciences, Faculty of Sciences, University of Gabes, Gabes, Tunisia and [2]Department of Engineering 'Enzo Ferrari', University of Modena and Reggio Emilia, Modena, Italy

Abstract

This study investigates the potential of six illite-rich clay samples from the Lower Cretaceous outcrops of Zemlet El Beidha (southern Tunisia) as precursors for geopolymer synthesis. The raw materials are predominantly illitic, although kaolinite remains a main reactive phase. Samples BHG_2 and BHG_5 were specifically selected for further investigation due to their relatively high kaolinite content compared to the remaining samples and due to their distinct secondary mineralogy, with BHG_2 being rich in hematite and BHG_5 being rich in calcite. This selection allowed for a comparative analysis of how different impurities affect geopolymerization. The samples were calcined at 550°C, 750°C and 950°C to determine the optimal dehydroxylation temperature. Alkali activation was systematically performed using 10, 12 and 14 M NaOH solutions to assess the influence of alkalinity on the polycondensation process. The 12 M NaOH was most effective for the dissolution of aluminosilicate phases without the detrimental effects of excess sodium. Structural characterization (X-ray diffraction, Fourier-transform infrared spectroscopy and scanning electron microscopy) confirmed that the greatest compressive strength (~8 MPa) was achieved with BHG_5 calcined at 750°C. Although this strength is lower than that of kaolinite-based geopolymers, it meets the requirements for non-structural applications, such as thermal insulation or lightweight masonry units. This research demonstrates a viable pathway for valorizing abundant illitic-kaolinitic Tunisian clays into sustainable construction materials.

Keywords: Clay characterization; geopolymers; illitic-kaolinitic clay; sodium hydroxide; southern Tunisia; thermal treatment

(Received 7 August 2025; revised 27 March 2026; accepted 7 April 2026; Associate Editor: Javier Cuertas)

In recent decades, the Tunisian construction sector has expanded rapidly, often without sufficient consideration for energy efficiency or environmental impacts. This growth has increased significantly energy consumption and greenhouse gas emissions. Consequently, there is an urgent need for research on cost-effective, alternative materials with lower environmental impacts.

Tunisia possesses significant clay potential, such as the deposits found in the Zemlet El Beidha region in the south-west. Although it is possible to obtain binders from alkali-activated clays, known as 'geopolymers' (Davidovits, 1991; Ounissi *et al.*, 2020), most existing studies have focused on high-purity precursors such as metakaolin (Davidovits, 2008; Autef *et al.*, 2013). However, there is a clear research gap regarding the valorization of complex, heterogeneous natural clays from specific Tunisian deposits. Although earlier research has extensively dealt with pure kaolinitic systems, this study examines the complex synergy between illite and the high concentrations of iron and calcium oxides specific to these raw Tunisian materials. This work aims to assess the feasibility of synthesizing geopolymers from two distinct illitic-kaolinitic clays: one hematite-rich (BHG_2) and one calcite-rich (BHG_5).

By contrasting these local resources with standard benchmarks, this research clarifies how their specific mineralogical composition and thermal activation (550°C, 750°C and 950°C) influence the formation of a consolidated binder. These eco-materials are refractory, inorganic polymers formed from both aluminium and silicon sources containing AlO_4^{5-} and SiO_4^{4-} tetrahedral units under highly alkaline conditions (NaOH, KOH, CsOH) at ambient temperature to obtain an amorphous three-dimensional network (Davidovits, 2002, 2008). The final product is directly dependent on two main factors: the source of the aluminosilicate and the nature of the activator.

The synthesis of geopolymeric materials relies on various aluminosilicate sources. Although pure metakaolin is widely used (Davidovits, 2008; Autef *et al.*, 2013), other more abundant materials, such as natural clays (Barone *et al.*, 2020; Vasic *et al.*, 2022; Zibret *et al.*, 2023) and certain industrial wastes, are also viable options. Furthermore, several studies have focused on the thermal activation of illitic-kaolinitic clays at temperatures ranging from 550°C to 950°C to produce geopolymers (Essaidi *et al.*, 2014a; Louati *et al.*, 2016; Ben Messaoud *et al.*, 2018a, 2018b; Hamdi *et al.*, 2019; Ounissi *et al.*, 2020; Derouiche *et al.*, 2023; Luzu *et al.*, 2024;

Corresponding author: Zainab Jrad; Email: nourizaynab@gmail.com

Cite this article: Jrad Z, Genua F, Lancellotti I, Leonelli C and Mahmoudi S (2026) Potential use of clays from Zemlet El Beidha (southern Tunisia) as aluminosilicate precursors for geopolymer synthesis. *Clay Minerals* **61**, 177–192. https://doi.org/10.1180/clm.2026.10034

Zerzouri *et al.*, 2025). However, these aluminosilicate sources often contain associated minerals such as quartz, hematite, calcite and dolomite. If these impurities are reactive in alkaline media, they can induce side reactions concurrent with the geopolymerization process (Autef *et al.*, 2013), forming multiple networks. Conversely, if the impurities are inert within the alkaline medium, they act as mineral reinforcements in the geopolymer matrix (Essaidi *et al.*, 2014b; Ben Messaoud *et al.*, 2018b). Such contaminants are Ca-bearing compounds, frequently occurring as calcite ($CaCO_3$) or dolomite ($CaMg(CO_3)_2$). Depending on its crystalline form, calcium may either react in alkaline media, as with CaO and $Ca(OH)_2$, or remain inert, as in the case of $CaCO_3$. Thermal activation of carbonate clays may result in the decomposition of these minerals, yielding reactive calcium (Gharzouni *et al.*, 2017; Karunadasa *et al.*, 2019; Yamchelou *et al.*, 2020).

The alkaline activator is a critical component in the geopolymerization process; depending on its quantity and concentration, it promotes the initial reaction stage and determines the final structure of the cured material (Duxson *et al.*, 2007). The most commonly used activators are hydroxides or alkaline salts, specifically sodium hydroxide (NaOH) and potassium hydroxide (KOH). Theoretically, a KOH solution would provide greater dissolution due to its higher alkalinity (Duxson *et al.*, 2005). However, in practice, NaOH exhibits a greater capacity to release silicate and aluminate monomers (Sumajouw & Rangan, 2006). The quantity of dissolved units depends on the type and concentration of alkali-activating solution, the temperature and the amorphous nature of the aluminosilicate source (Van Riessen & Chen-Tan, 2013). The clays used in this study originate from the Lower Cretaceous or Bouhedma Formation of the Zemlet El Beidha region (Gabes Governorate, Tunisia). This formation consists of alternating red and green clays, which are slightly gypsiferous in the upper part of the deposit (Boussen *et al.*, 2016). In particular, illitic-kaolinitic clays have shown promising properties for building ceramics (Escalera *et al.*, 2014; Mahmoudi *et al.*, 2016). Therefore, this type of clay warrants investigation as an aluminosilicate source for the synthesis of consolidated materials at low temperatures.

With a view towards sustainable regional development, this study aims to identify clays that night potentially be used to synthesize a geopolymeric binder. The synthesized solid products were characterized by X-ray diffraction (XRD), Fourier-transform infrared (FTIR) spectroscopy and scanning electron microscopy (SEM), as well as with compressive strength tests.

Materials and methods

Raw materials

Six Tunisian clay samples were collected from the Zemlet El Beidha site in the Gabes region to be used as aluminosilicate sources for the synthesis of alkali-activated materials. These samples, labelled BHG_1 to BHG_6, were extracted sequentially from the base to the top of the Bouhedma Formation. This formation, which constitutes the core of the Zemlet El Beidha anticline, consists of alternating red and green clay layers that become slightly gypsiferous towards the top. Specifically, samples BHG_1 through BHG_3 correspond to the red clays, while samples BHG_4 through BHG_6 correspond to the green clays. The clay samples were dried at 80°C until a constant weight was achieved, then they were crushed and sieved to a particle size of <200 µm. Representative samples BHG_2 and BHG_5 were selected for calcination at three different temperatures (550°C, 750°C and 950°C) for 4 h. These temperatures were selected based on prior thermogravimetric analysis (TGA)/differential thermal analysis (DTA) of the raw clay. Following thermal treatment, the calcined powders were sieved to a particle size of <200 µm to eliminate any agglomerates and to ensure particle fineness. Hereafter, the untreated clays are labelled $BHG_1{}^{25}$, $BHG_2{}^{25}$, $BHG_3{}^{25}$, $BHG_4{}^{25}$, $BHG_5{}^{25}$ and $BHG_6{}^{25}$, whereas the thermally treated samples are designated $BHG_2{}^{\theta}$ and $BHG_5{}^{\theta}$, where θ represents the specific calcination temperature (e.g. $BHG_2{}^{550}$ denotes the BHG_2 clay calcined at 550°C).

The alkali-activated clays yielded consolidated materials designated as ${}^{NaOH}GBHG_2{}^{\theta}$ and ${}^{NaOH}GBHG_5{}^{\theta}$, where G refers to the geopolymeric state, BHG_2 and BHG_5 correspond to the source clays and θ denotes the calcination temperature. The superscript prefix NaOH represents the molar concentration of the sodium hydroxide solution (10, 12 or 14 M). For instance, the sample labelled ${}^{10}GBHG_2{}^{750}$ identifies a geopolymer synthesized from red clay BHG_2 calcined at 750°C using a 10 M NaOH activator solution. This solution was prepared 24 h prior to use by dissolving NaOH pellets (96% purity) in distilled water to achieve the required molarity.

Sample preparation

Sample synthesis was carried out in two stages. In the first stage, alkaline-activating solutions with molarities of 10, 12 and 14 M were prepared by dissolving NaOH pellets in distilled water. The solutions were allowed to cool to ambient temperature prior to use. In the second stage, the aluminosilicate precursor (either raw or calcined clay) was gradually incorporated into the alkaline activator. A liquid-to-solid (L/S) mass ratio of 0.7 was maintained to ensure adequate workability of the resulting paste. The mixture was manually homogenized for 3–5 min until a uniform paste was obtained. The fresh paste was immediately cast into closed polystyrene moulds and manually vibrated to minimize entrapped air voids. The specimens were cured at 60°C for 24 h, following the synthesis parameters adapted from Autef *et al.* (2013). After curing, the samples remained in their moulds at room temperature for an additional 48 h before demoulding. Finally, the specimens were stored under laboratory conditions for 28 days prior to characterization and compressive strength testing, in accordance with the protocols described by Hamdi *et al.* (2019).

Characterization techniques

The chemical composition of the raw clays was determined by X-ray fluorescence (XRF) using an X-MET 5100 (Oxford Instruments) spectrometer. The samples were prepared as pressed pellets and measured with a fixed runtime of 180 s. The results were validated by comparison with certified standards. The loss on ignition (LOI) was determined from the weight difference between samples heated at 100°C and 1000°C for 2 h.

The particle-size distributions of untreated and calcined clays were determined by laser diffraction using a Malvern Mastersizer 3000 equipped with a Hydro S wet dispersion unit. Samples were dispersed in water containing sodium hexametaphosphate as a deflocculant. Measurements were performed within a range of 0.05–880 µm, maintaining an obscuration of 5–10% to prevent particle agglomeration. The specific surface area (SSA) was determined using two complementary methods to account for both textural porosity and clay swelling. External SSA and porosity were measured by N_2 adsorption at 77.3 K (Brunauer–Emmett–Teller

https://doi.org/10.1180/clm.2026.10034 Published online by Cambridge University Press

(BET) method) using a Micromeritics Gemini 2380 instrument, following degassing at 110°C. Total SSA (internal and external) was evaluated *via* the methylene blue (MB) adsorption method (NF P 94-068, 1998). A 10 g 100 mL^{-1} clay-to-water suspension was titrated with a 10 g L^{-1} MB solution, using the spot test on filter paper method to determine the adsorption capacity.

Elemental composition was determined using a Thermo Scientific FlashSmart analyser *via* high-temperature combustion (950–1800°C) in an oxygen-rich environment. Ground samples (1–2 mg) were placed in tin capsules with vanadium pentoxide (V_2O_5) as a combustion catalyst. The resulting gases were separated by gas chromatography and quantified using a thermal conductivity detector. System calibration was validated using certified methionine and cystine standards.

The mineralogical composition of the samples was identified by XRD with a Brucker AXS D8 Advance Diffractometer using a Cu-*K*α radiation source (λ = 0.154186 Å). The patterns were recorded over a 5–60°2θ range with a step size of 0.02° and a scan speed of 2° min^{-1}.

To monitor the structural changes during geopolymerization, FTIR spectra were recorded between 500 and 4000 cm^{-1} with a resolution of 4 cm^{-1}. Two different sampling techniques were employed: attenuated total reflectance (ATR) mode for the raw clays and the KBr pellet method for the geopolymer samples after 28 days of curing. Measurements were conducted using a Frontier Nicolet 380 spectrometer. All resulting spectra were baseline-corrected and normalized using the *OMNIC* software package.

The cation-exchange capacity (CEC) was determined using the copper-ethylenediamine (Cu- EDA) method. Briefly, 1 g of clay was dispersed in 8 mL of 0.05 M Cu-EDA and diluted to 20 mL. After 1 h of agitation and centrifugation, 15 mL of the supernatant was treated with 5 mL of 0.5 M HCl and 2 g of KI. The liberated iodine (I_2) was titrated against 0.05 M $Na_2S_2O_3$ until decolourization. The results are expressed in meq 100 g^{-1}. The plastic behaviour of the clay samples was characterized by determining the Atterberg limits using the Casagrande method (LCPC, 1987; Nagendra *et al.*, 2022). These tests were performed on the <400 μm fraction. The liquid limit (LL) and plastic limit (PL) were determined according to NF P 94-052-1 and NF P94-051 standards, respectively (AFNOR, 1995).

Simultaneous TGA/DTA was performed using a Netzsch STA 429 analyser (Selb, Germany). Samples were heated in a platinum (Pt) crucible from ambient temperature to 1400°C at a constant rate of 10°C min^{-1} under a continuous flow of dry air. Compressive strength was determined using a Lloyd Instruments EZ20 tester at a crosshead speed of 0.1 mm min^{-1} on cylindrical geopolymer specimens (26 mm in diameter and 40 mm in height). Before testing, specimens were dry-polished to ensure they had flat and parallel surfaces.

Microstructural and compositional characterization of the geopolymer matrices was conducted using environmental SEM (Quanta 200, FEI Company) operating under high vacuum, coupled with an energy-dispersive x-ray spectroscopy (EDS) system.

Results and discussion

Physicochemical and structural characterization of the raw clays

Six clay samples, designated as BHG_1 through BHG_6, were characterized to evaluate their suitability as aluminosilicate precursors for geopolymerization.

The particle-size distribution (Table 1) showed three distinct size fractions: clay (<2 μm, 14–46%), silt (2–20 μm, 52–80%) and coarser particles (>20 μm, 0.6–12%). Although all raw materials were ground to under 200 μm, the fraction exceeding 20 μm corresponding to fine silt or very fine sand remained well below the maximum grinding limit. Among the investigated samples, BHG_2 exhibited the highest silt content (80%). This specific granulometry is known to promote denser particle packing and to increase reactivity during the geopolymerization process, which is consistent with previous observations in kaolinitic-illitic systems (Allahverdi & Kani, 2009; Cong *et al.*, 2016; Merabtene *et al.*, 2019).

The SSA, determined by MB adsorption and BET methods (Mahmoudi *et al.*, 2016; Michot, 2018), ranged from 146 m^2 g^{-1} (BHG_5) to 199 m^2 g^{-1} (BHG_2; Table 1). Illite was the predominant mineral phase across all samples. The observed variations in SSA for sample BHG_2 are consistent with values reported in the literature for illite-rich (Cong *et al.*, 2016; Rahier *et al.*, 2018) and non-expansive clays. This property is controlled by a finer particle-size distribution and a higher proportion of silt-sized particles (2–20 μm), which contribute to an increased external surface area.

Furthermore, the BET surface area varied between 28.7 m^2 g^{-1} (BHG_1) and 74 m^2 g^{-1} (BHG_6). The higher BET values observed for the green clays (BHG_4–BHG_6) are probably associated with the synergistic effects of their textural properties and carbonate contents rather than mineralogy alone. The CEC values ranged from 22 to 29 meq 100 g^{-1} (Table 1), which is in good agreement with the established literature for illite-dominated clays (typically 20–35 meq 100 g^{-1}; Allahverdi & Kani, 2009; Merabtene *et al.*, 2019; Lahoti *et al.*, 2020). The relatively narrow range of CEC values across all samples reflects the mineralogical predominance of illite. However, the slightly higher CEC observed in samples with a more significant <2 μm fraction (BHG_4–BHG_6) is attributed to their higher SSA rather than a shift in mineralogical species. Regarding the chemical environment, the green clays (BHG_4–BHG_6) exhibited alkaline pH values ranging from 8.5 to 8.8, attributed to the abundance of calcite. In contrast, the red clays (BHG_1–BHG_3) showed near-neutral pH values between 6.6 and 7.8.

Plasticity index (PI) values range from 17% to 36%, and LL values range from 42% to 64% (Table 1), indicating moderate plasticity. These samples fall within the illitic domain, as illustrated in the Holtz & Kovacs (1981) diagram (Fig. 1). Sample BHG_6 displayed the highest PI (36%), which correlates with its greater clay fraction (46%). The plasticity of these deposits is closely governed by their mineralogical composition, where an increase in illite content leads to higher plasticity (Fig. 1), which is in good agreement with Ben M'barek-Jemaï *et al.* (2025). Furthermore, this classification confirms the absence of highly expansive smectitic clays, thereby supporting the suitability of these materials for geopolymer synthesis.

The chemical composition (Table 2) shows significant SiO_2 concentrations (36–57 wt.%), primarily attributed to free quartz and, to a lesser extent, 2:1 clay minerals (Coulibaly *et al.*, 2020). The Al_2O_3 contents vary between 14 and 17 wt.%, resulting in SiO_2/Al_2O_3 ratios exceeding 2. This high ratio stems from the abundance of free SiO_2, which is characteristic of the detrital input in this depositional environment (Ben M'barek-Jemaï *et al.*, 2025). Furthermore, red clays are characterized by elevated Fe_2O_3 levels (7.03–12.33 wt.%) due to hematite, whereas green clays exhibit high CaO contents (10.42–23.35 wt.%) associated with calcite. The LOI at 1000°C (11.96–15.55 wt.%) reflects the combined effects of clay mineral dehydroxylation, carbonate decomposition

https://doi.org/10.1180/clm.2026.10034 Published online by Cambridge University Press

Table 1. Physical and geotechnical properties of the raw clay samples.

	Granulometry (±1 wt.%)			Physical tests				Plasticity (±2 wt.%)		
	<2 µm	2–20 µm	>20 µm	pH	CEC (meq 100 g^{-1})	SSA (m^2 g^{-1})	S_{BET} (m^2 g^{-1})	LL	PL	PI
BHG_1	15	72	12	6.6	28.0	167	28.7	51	25	26
BHG_2	14	80	5	7.0	22.6	199	30.5	49	28	20
BHG_3	19	74	6	7.8	26.6	178	41.3	42	25	17
BHG_4	41	56	1	8.8	26.6	199	70.0	49	26	23
BHG_5	44	52	4	8.5	26.6	146	66.2	47	24	22
BHG_6	46	53	0.6	8.7	29.3	157	74.0	64	28	36

PI = plasticity index; S_{BET} = BET specific surface area.

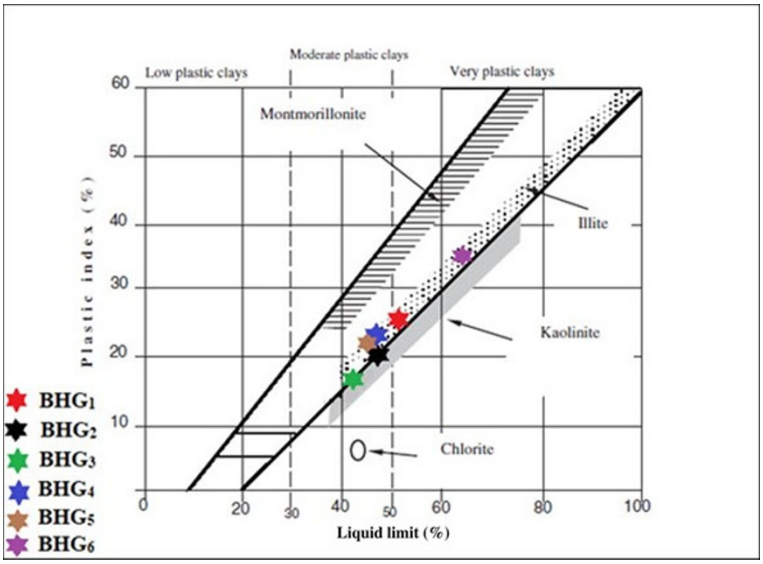

Figure 1. Projection of the studied clay samples on the Holtz and Kovacs diagram (adapted from Holtz & Kovacs, 1981).

Table 2. Chemical composition of the raw clays obtained by XRF (±0.01 wt.%).

	Sample					
Oxide (%)	BHG_1	BHG_2	BHG_3	BHG_4	BHG_5	BHG_6
SiO_2	57.25	49.88	49.24	45.10	36.47	48.02
Al_2O_3	16.33	17.78	15.71	14.61	15.02	14.20
Fe_2O_3	7.03	12.33	8.80	5.51	3.59	6.06
K_2O	3.57	3.97	4.28	4.55	3.66	4.88
Na_2O	<0.003	<0.003	<0.003	<0.003	<0.003	<0.003
MgO	2.36	2.19	2.35	3.29	2.53	3.55
CaO	0.07	0.55	5.36	10.42	23.35	8.08
TiO_2	0.93	0.94	0.65	0.45	0.30	0.47
LOI (±0.01 wt.%)	11.96	12.05	13.29	15.55	14.55	14.33
SiO_2/Al_2O_3 (w/w)	3.50	2.80	3.13	3.08	2.42	3.38
C_{total} (±0.01 wt.%)	0.10	0.10	1.14	2.64	4.90	2.12

and organic matter combustion (El Boukili *et al.*, 2021), as supported by the exothermic signals in the differential scanning calorimetry (DSC) curves. Total carbon analysis reveals that samples BHG_4[25], BHG_5[25] and BHG_6[25] have the highest carbon contents, with BHG_5[25] exhibiting the maximum value. These results correlate with XRF data (Table 2), confirming a high carbonate abundance, which accounts for the elevated pH values observed (8.5–8.8; Table 1).

The XRD traces (Fig. 2) and FTIR spectra (Fig. 3) identified illite (International Centre for Diffraction Data (ICDD) reference trace: 00-002-0462) as the dominant phase, ranging from 61 to 96 wt.%. Kaolinite (04-013-2830) was a secondary component (4–39 wt.%; Table 3). Additionally, minor phases of quartz (04-012-0490), hematite (04-008-8479), calcite (01-089-5862) and dolomite (01-075-1766) were detected. Kaolinite was identified by its diagnostic FTIR bands, including the Al–OH bending doublets at 909 and 911 cm^{-1}, the Al–OH stretching vibration at 3698 cm^{-1} and Si–O vibrations near 798 cm^{-1}, in agreement with previously published data (Zhang *et al.*, 2012; Dehmani *et al.*, 2026). Illite was identified by the band at 3620 cm^{-1} (Hajjaji, 2014; D'Elia *et al.*, 2018; Luzu *et al.*, 2024). Additionally, all samples exhibited a broad absorption band between 975 and 997 cm^{-1}, attributed to

https://doi.org/10.1180/clm.2026.10034 Published online by Cambridge University Press

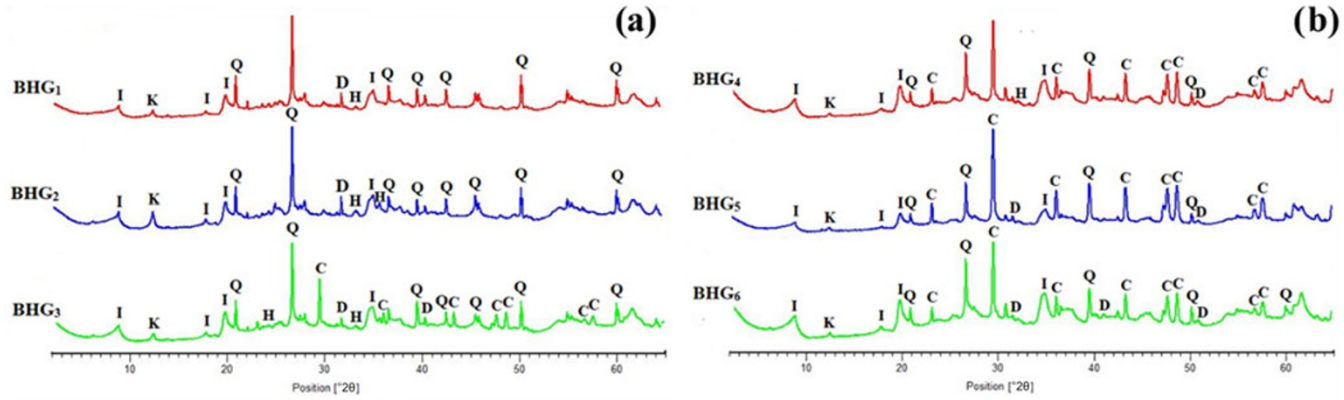

Figure 2. XRD traces of (a) red and (b) green clay samples. C = calcite; D = dolomite; H = hematite; I = illite; K = kaolinite; Q = quartz.

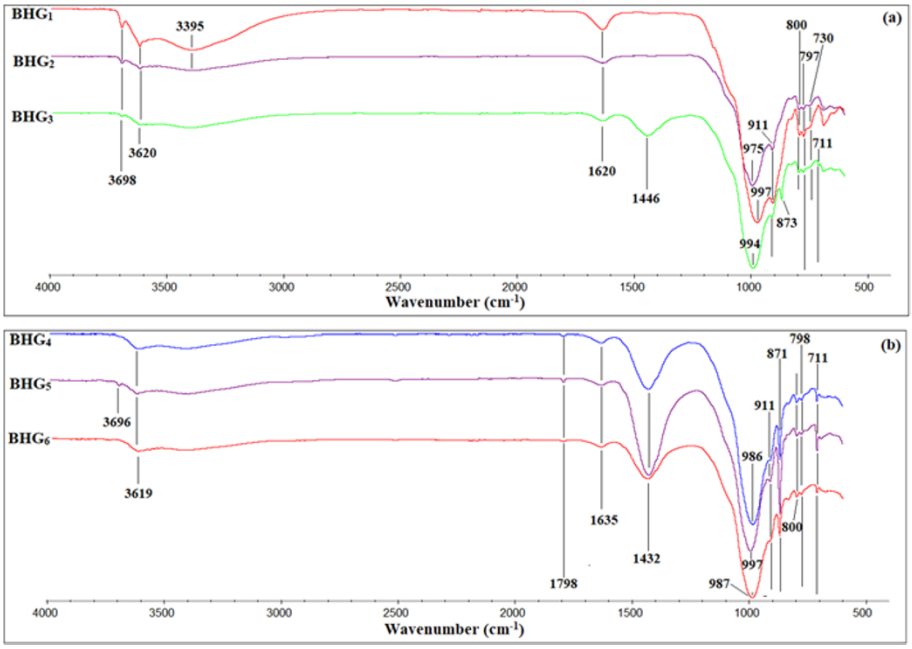

Figure 3. ATR-FTIR spectra of (a) red and (b) green raw clay samples.

Table 3. Mineralogical composition (±3 wt.%) of the raw clay samples.

						Fraction (<2 μm)	
Sample	Phyllosilicate	Quartz	Calcite	Dolomite	Hematite	Illite	Kaolinite
BHG_1	67	30	–	1	2	78	22
BHG_2	51	43	–	3	3	61	39
BHG_3	66	20	12	–	2	87	13
BHG_4	71	7	20	2	–	92	8
BHG_5	32	8	55	5	–	79	21
BHG_6	74	7	17	2	–	96	4

Si–O stretching vibrations in the silicates. Other detected features included the quartz doublet (Mezni *et al.*, 2011) at 797–800 cm^{-1} and a band at 1620 cm^{-1} corresponding to the H–O–H scissor bending vibrations of adsorbed water (Dehmani *et al.*, 2026).

For the carbonate-rich samples (BHG425, BHG525 and BHG625), the spectra retained the signatures of kaolinite and quartz but exhibited additional bands at 1798, 1432 and 730 cm^{-1}, indicative of dolomite (Ji *et al.*, 2009; Ionescu *et al.*, 2025). Furthermore, bands at 873 and 711 cm^{-1} confirmed the presence of calcite (Reig *et al.*, 2002; Ionescu *et al.*, 2025). Notably, the higher intensity of the 1432 cm^{-1} carbonate band in sample BHG525 reflects a greater calcium content relative to BHG425 and BHG625, which is in excellent agreement with the XRF results (Table 2).

The thermal behaviour of the raw clays was investigated using simultaneous TGA/DTA analysis up to 1400°C (Fig. 4). All samples exhibited a first common endothermic peak at

https://doi.org/10.1180/clm.2026.10034 Published online by Cambridge University Press

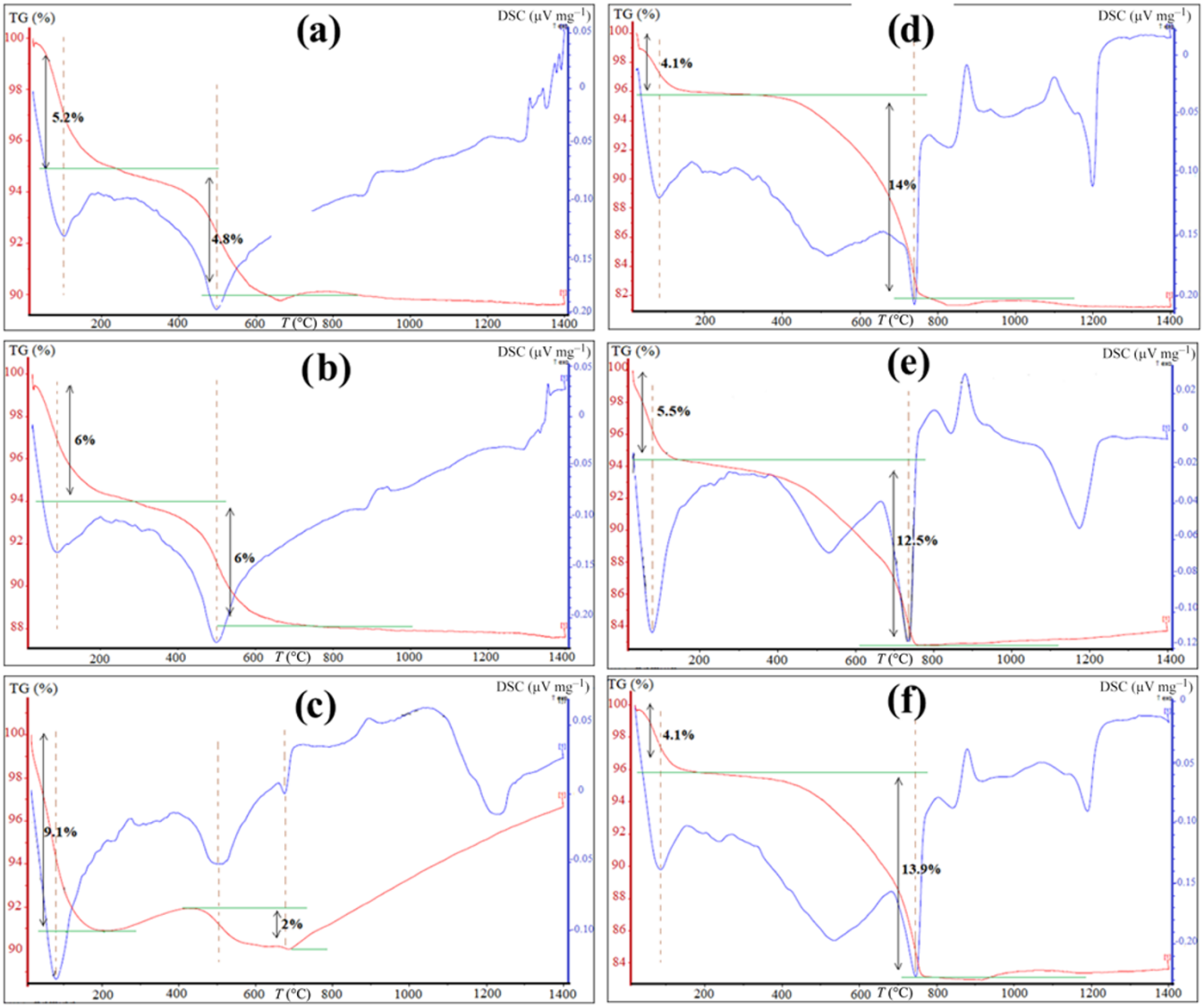

Figure 4. Thermal analysis of raw clays: (a) BHG_1^{25}, (b) BHG_2^{25}, (c) BHG_3^{25}, (d) BHG_4^{25}, (e) BHG_5^{25} and (f) BHG_6^{25}. The horizental green lines denote the baselines used to determine the mass loss steps for each thermal event. TG = thermogravimetry.

90–115°C (e.g. 115°C in BHG_1^{25}; Fig. 4a), corresponding to the release of physically adsorbed water and weakly bound interparticle/interlayer water associated with clay mineral surfaces (D'Elia *et al.*, 2018). A second major endothermic effect occurred between 450°C and 600°C (e.g. 548°C in BHG_2^{25}; Fig. 4b). This thermal event is mainly related to the dehydroxylation of illite, which occurs over a broad temperature range. A minor contribution from kaolinite dehydroxylation (Ilić *et al.*, 2010; Elimbi *et al.*, 2011; Polcowñuk Iriarte *et al.*, 2025), typically observed between 450°C and 550°C, cannot be excluded where kaolinite is present as a secondary phase. This interpretation is consistent with the predominance of illite identified by XRD and with recent thermal studies of clay minerals (Do Nascimento & Schaefer, 2021). Distinct thermal behaviours were observed among the samples. Sample BHG_2^{25} (Fig. 4b) showed an additional endothermic peak at 300°C, assigned to goethite dehydroxylation ($FeOOH \rightarrow Fe_2O_3 + H_2O$) (Foldvari, 2011), consistent with its elevated Fe_2O_3 content (12.33 wt.%; Table 2). In contrast, BHG_4^{25}, BHG_5^{25} and BHG_6^{25} (Fig. 4d–f) displayed pronounced endothermic effects at ~750°C, confirming calcite decomposition (Sdiri *et al.*, 2010; Pulidori *et al.*, 2022; Rat *et al.*, 2022), in agreement with their high CaO contents (10.42–23.35 wt.%; Table 2) and proportions of calcite (17–55 wt.%; Table 3). A minor endothermic peak at 573°C without associated mass loss corresponds to the α- to β-quartz transition (El Boukili *et al.*, 2021), reflecting the ubiquitous presence of quartz in all samples. Interestingly, the characteristic exothermic peak near 950°C related to the metakaolinite-to-mullite transformation was conspicuously absent from BHG_6^{25}. This is probably due to its low kaolinite content (4 wt.%; Table 3) and the inhibitory effects of impurities such as iron oxides (Fe_2O_3: 6.06 wt.%; Table 2) and calcium carbonate (Chalouati *el al.*, 2021; Derouiche *et al.*, 2023).

Above 1000°C, the DTA curves showed an endothermic trend peaking at ~1200°C. Although the formation of primary mullite occurs at lower temperatures (~ 980°C), this high-temperature endothermic event is probably associated with the formation of

https://doi.org/10.1180/clm.2026.10034 Published online by Cambridge University Press

Table 4. Particle-size distributions (±1 wt.%), MB SSA and BET specific surface area (S_{BET}) of BHG_2^{25} and BHG_5^{25} at various calcination temperatures.

	BHG_2				BHG_5			
Calcination temperature (°C)	25	550	750	950	25	550	750	950
<2 µm	14	4	2.6	0.4	44	1	1	0
2–20 µm	80	45	41	24	52	15	16	11
>20 µm	5	50	56	75	4	84	83	89
SSA ($m^2\ g^{-1}$) ± 1	199	58	21	5	146	42	24	6
S_{BET} ($m^2\ g^{-1}$) ± 1	30.5	47.0	24.7	0.4	66.2	53.6	24.0	0.8

a liquid phase (eutectic melting) and the potential growth of secondary mullite within the melt. In sample BHG_5, the presence of CaO (from calcite decarbonation) acted as an effective flux, lowering the melting point of the Si–Al system and promoting the development of a vitreous phase. This interpretation is consistent with recent studies on the firing behaviour of calcareous illitic clays (Chalouati *et al.*, 2021; Martínez-Martínez *et al.*, 2023; Ionescu *et al.*, 2025), where the interaction between CaO and the aluminosilicate matrix induces partial melting in the 1150–1250°C range. These thermal results corroborated the mineralogical interpretations obtained from XRD and XRF analyses and guided the selection of calcination temperatures of 550°C, 750°C and 950°C.

Based on their kaolinite content (BHG_2^{25}: 39%; BHG_5^{25}: 21%) and thermal reactivity, samples BHG_2^{25} (hematite-rich) and BHG_5^{25} (calcite-rich) were selected for calcination. The selected temperatures corresponded to specific thermal events: kaolinite dehydroxylation at 550°C (Zhang *et al.*, 2022), carbonate decomposition at 750°C (D'Elia *et al.*, 2018; Rat *et al.*, 2022) and illite dehydroxylation at 950°C (Csáki *et al.*, 2022).

Effects of thermal treatment on the selected clays

The calcination process induced progressive particle agglomeration, with significant coarsening observed above 550°C (Chandrasekhar & Ramaswamy, 2002; Konan *et al.*, 2006; Hedfi *et al.*, 2014). This effect was particularly pronounced in BHG_5, which showed a nearly complete disappearance of its fine fraction (<2 µm) at 950°C (see Table 4), as sintering processes became dominant (Derouiche *et al.*, 2023). Thermal treatment caused a marked reduction in SSA with increasing temperature, demonstrated by the decrease from 199 to 5 $m^2\ g^{-1}$ for BHG_2 and from 146 to 6 $m^2\ g^{-1}$ for BHG_5. These changes reflect a denser particle packing and microstructural consolidation through sintering (Hollanders *et al.*, 2016).

XRD traces (Fig. 5a,b) confirmed kaolinite dehydroxylation at 550°C *via* the collapse of the 7.15 Å peak, resulting in the formation of poorly crystalline metakaolin (Fabbri *et al.*, 2013). Simultaneously, dolomite decomposition released reactive CaO/MgO (Cheng & Specht, 2006). Although illite reflections persist at this temperature, the mineral undergoes dehydroxylation to form meta-illite, a process typically initiating at ∼500°C. By 750°C, the complete decarbonation of calcite in BHG_5 significantly enhanced the amorphous halo (15–40°2θ; D'Elia *et al.*, 2018; Rat *et al.*, 2022), indicating a state of maximum structural disorder. At this stage, the high reactivity of the newly formed CaO, combined with the disordered silica from the clay precursors, favoured the early crystallization of various calcium-bearing minerals such as wollastonite ($CaSiO_3$; Dathe *et al.*, 2021). Finally, at 950°C, illite decomposition promoted the crystallization of mullite, plagioclase and diopside in BHG_5 through solid-state reactions (Csáki *et al.*, 2022), whereas in BHG_2 illite was no longer detected (Escalera *et al.*, 2014).

FTIR spectroscopy corroborated these mineralogical changes (Fig. S1). The disappearance of kaolinite's Al–OH bands (3695, 3620 and 913 cm^{-1}) at 550°C confirmed dehydroxylation. Simultaneously, the broadening and shifting of the main Si–O–Si stretching band (initially at 1031 cm^{-1}) indicated the collapse of the long-range crystalline order and the formation of a highly disordered metakaolin structure (Prud'homme *et al.*, 2013). For BHG_5, the calcite bands (1432 and 873 cm^{-1}) vanished at 750°C, confirming decarbonation (D'Elia *et al.*, 2018), whereas the quartz signatures (797–779 cm^{-1}) remained unaltered (Hajjaji *et al.*, 2010; Souri *et al.*, 2015). These transformations establish a reactivity hierarchy: 750°C maximized the structural amorphization by balancing metakaolin formation with carbonate decomposition. Conversely, firing at 950°C promoted the initial nucleation of primary mullite, leading to a partial reorganization on the network and a reduction in soluble phases (Zhang *et al.*, 2022). This explains the optimal geopolymer performance of BHG_5 calcined at 750°C (see the 'Compressive strength' section below), underscoring the critical link between thermal history, structural disorder and alkali activation potential.

Comparative phase evolution in BHG_5 and BHG_2 geopolymer systems under variable alkaline activation

XRD analyses were conducted on consolidated geopolymer specimens after 28 days of curing (Fig. S2) to assess the influence of raw material composition, calcination temperature and NaOH concentration on mineralogical development. Figure 6 illustrates the evolution of crystallinity and amorphization in systems derived from BHG_5 and BHG_2 clays.

For geopolymers based on BHG_5 clay, substantial structural transformations were observed. In the uncalcined sample $GBHG_5^{25}$, the intensity of the illite peak decreased as the activator concentration increased, indicating partial dissolution during alkaline activation (Fig. 6a). The disappearance of calcite peaks confirmed its degradation, whereas the emergence of zeolitic phases such as Na-faujasite ($(Na_2,Ca,Mg)_{3.5}(Al_7Si_{17}O_{48})\cdot 32H_2O$) and hydroxysodalite ($Na_{6+x}(AlSiO_4)_6(OH)_x\cdot nH_2O$) was identified at 12 and 14 M NaOH concentrations. These findings confirmed the crystallization of secondary phases favoured by calcium-rich precursors (Zibouche *et al.*, 2009; Vaičiukynienė *et al.*, 2016). Pirssonite ($Na_2Ca(CO_3)_2\cdot 2H_2O$) formed in the $^{12}GBHG_5^{25}$ and $^{14}GBHG_5^{25}$ specimens, as the interaction between calcite and sodium ions promoted the synthesis of hydrated double carbonates (Abdel-Gawwad & Abo-El-Enein, 2016). Finally, quartz remained unaltered, consistent with its inert nature (Lecomte *et al.*, 2003; Zibouche *et al.*, 2009). Calcination of BHG_5 at 550°C (Fig. 6b) led to kaolinite dehydroxylation and its transformation into metakaolin, as evidenced by the disappearance of its characteristic 7.15 Å reflection (Zhang *et al.*, 2022). The concurrent reduction in dolomite and calcite peak intensities suggested the

https://doi.org/10.1180/clm.2026.10034 Published online by Cambridge University Press

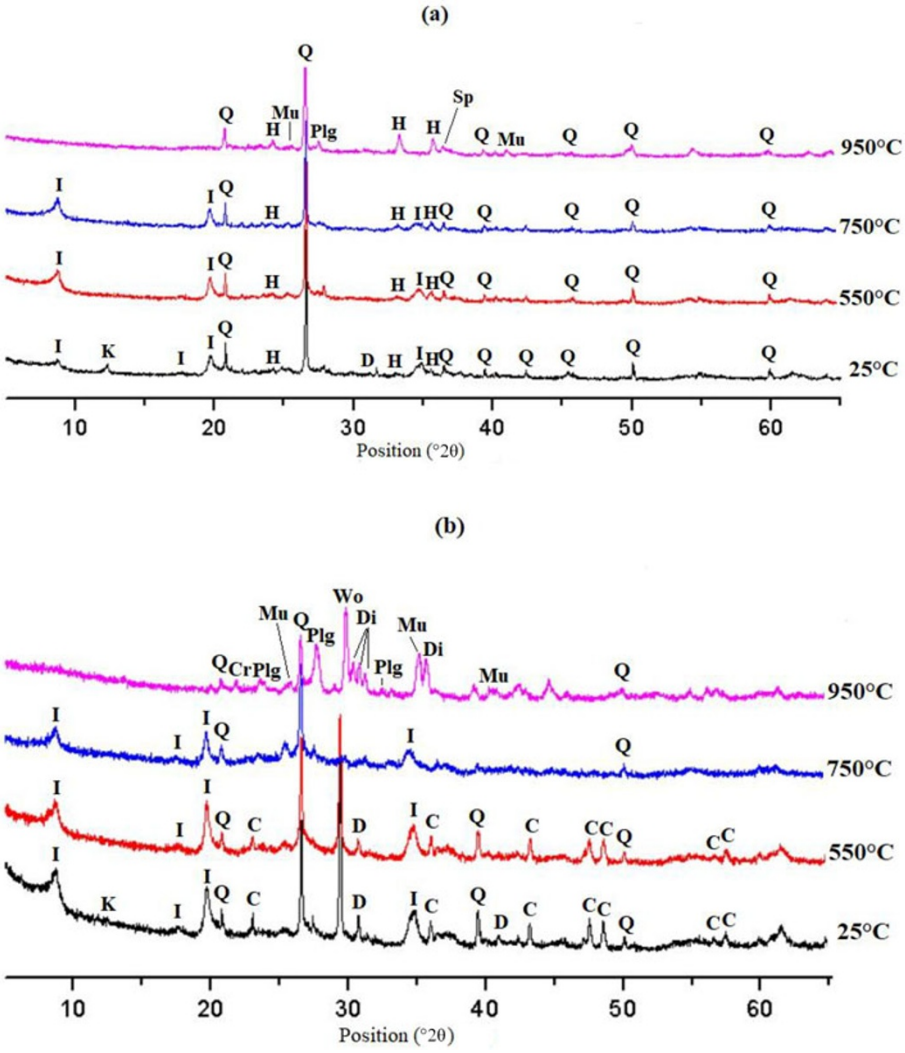

Figure 5. XRD traces of the selected clay samples before and after calcination: (a) BHG_2 and (b) BHG_5. C = calcite; Cr = cristobalite; D = dolomite; Di = diopside; H = hematite; I = illite; K = kaolinite; Mu = mullite; Plg = plagioclase; Q = quartz; Sp = spinel; Wo = wollastonite.

generation of reactive CaO and MgO. At 12 M NaOH, the formation of garronite ($Na_6(Al_6Si_{10}O_{32})\cdot 8.5H_2O$) and Na-faujasite indicated enhanced dissolution and the precipitation of zeolitic phases characteristic of calcium-rich systems (Stroscio *et al.*, 2024). The most pronounced structural reorganization occurred in BHG_5 specimens calcined at 750°C (Fig. 6c), which exhibited broad humps between 22°2θ and 43°2θ, attributed to amorphous material, and dominant hydrosodalite peaks. Increasing the NaOH molarity increased the crystal order, suggesting the progressive consumption of illite. Weak diffraction signals at 29.7°2θ and 34.5°2θ may correspond to portlandite (Mintsaev *et al.*, 2022; Stroscio *et al.*, 2024), although partial masking by amorphous phases prevents unambiguous identification. In contrast, calcination at 950°C yielded $GBHG_5^{950}$ specimens (Fig. 6d) rich in high-temperature phases, such as diopside, mullite and plagioclase (Mahmoudi *et al.*, 2010; Azzouz *et al.*, 2011), exhibiting negligible amorphous character and reduced reactivity. Compared to BHG_5-based systems, geopolymers derived from BHG_2 clay exhibited markedly lower crystal order and limited phase evolution. In uncalcined BHG_2^{25} specimens (Fig. 6e), kaolinite and illite peaks persisted regardless of the NaOH concentration, indicating incomplete dissolution. Activation with 12 M NaOH led to only a slight attenuation of clay peaks, while the amorphous hump between 20°2θ and 30°2θ remained faint, reflecting poor gel formation. BHG_2 calcined at 550°C and 750°C (Fig. 6f, g) displayed illite peaks as a result of its high thermal stability below 950°C (Ferone *et al.*, 2015).

Despite alkali activation, no significant transformation into amorphous or zeolitic phases occurred, denoting limited reactivity. Geopolymers from BHG_2 calcined at 950°C (Fig. 6h) revealed a crystalline matrix composed of quartz, plagioclase, hematite, spinel and mullite. The persistence of the quartz peaks confirmed its inert role, which explains the limited reactivity of BHG_2 regardless of the activation conditions (Escalera *et al.*, 2014). The increase in hematite intensity might have been related to an increase in its relative content following silicate decomposition rather than secondary iron oxide formation (Baccour *et al.*, 2008). Hydrosodalite was identified in trace amounts, consistent with minimal phase nucleation.

This mineralogical composition contrasts with BHG_5-based materials, where the abundance of calcite and reactive CaO promoted greater amorphization and zeolite formation. Overall, the XRD traces indicate that BHG_5-based geopolymers exhibited higher degrees of amorphization and crystalline phase diversification than those derived from BHG_2 (Fig. 6). This trend is particularly evident at intermediate calcination temperatures (750°C) and elevated NaOH concentrations.

https://doi.org/10.1180/clm.2026.10034 Published online by Cambridge University Press

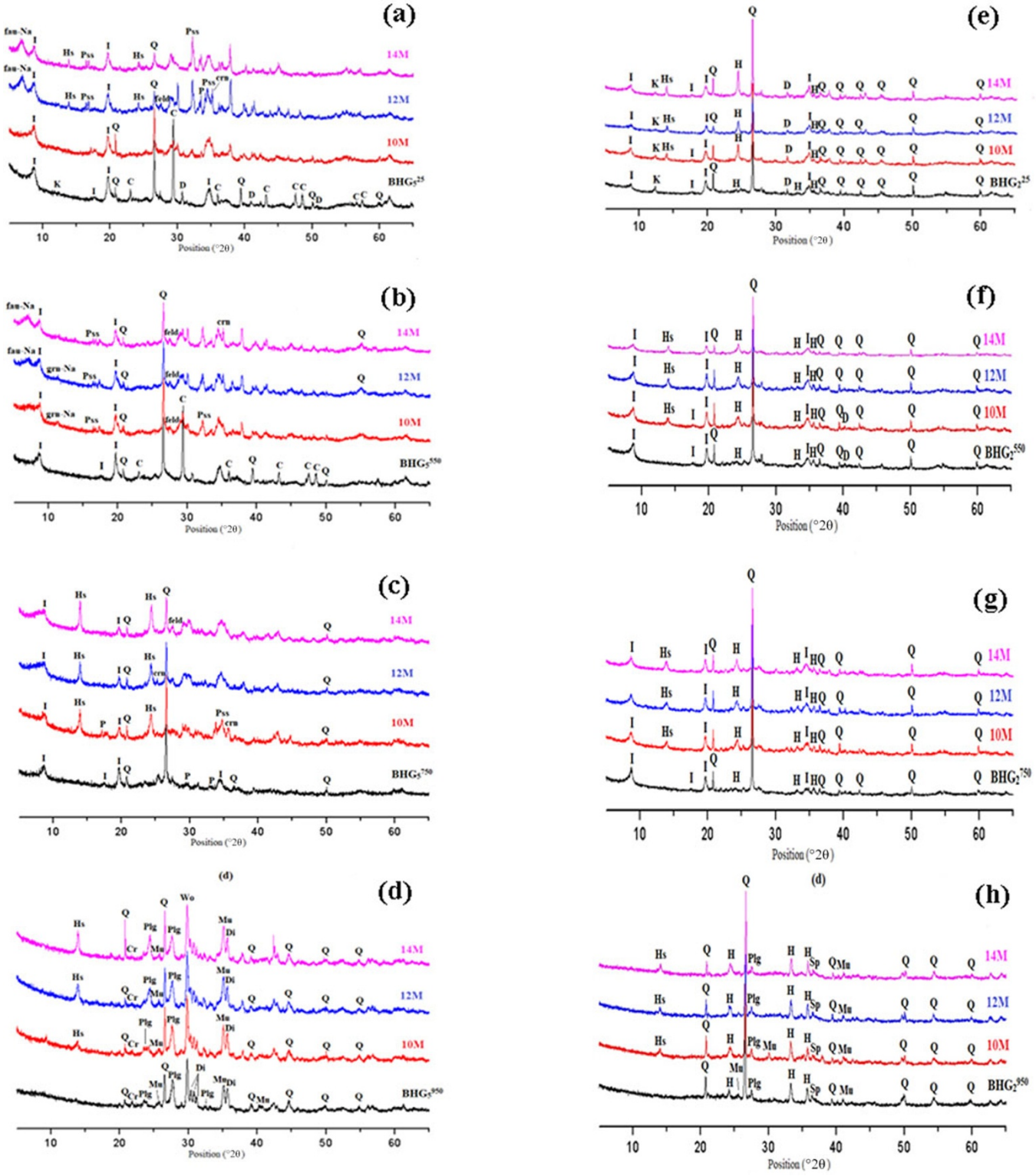

Figure 6. XRD traces of 28 day NaOH-activated pastes (10, 12 and 14 M) prepared from the bulk clays (a) BHG_5^{25}, (b) BHG_5^{550}, (c) BHG_5^{750}, (d) BHG_5^{950}, (e) BHG_2^{25}, (f) BHG_2^{550}, (g) BHG_2^{750} and (h) BHG_2^{950}. C = calcite; Cr = cristobalite; crn = corundum; D = dolomite; Di = diopside; fau-Na = Na-faujasite; feld = feldspars; grn-Na = garronite; H = hematite; Hs = hydrosodalite; I = illite; K = Kaolinite; Mu = mullite; P = portlandite; Plg = plagioclase; Pss = pirssonite; Q = quartz; Sp = spinel; Wo = wollastonite.

https://doi.org/10.1180/clm.2026.10034 Published online by Cambridge University Press

Structural evolution of BHG_5 and BHG_2 geopolymers via *FTIR spectroscopy*

The FTIR analysis was conducted to evaluate the structural evolution of geopolymer matrices derived from the BHG_5 and BHG_2 clays. These clays were heated at various calcination temperatures and activated using NaOH solutions of increasing concentration. Figure 7 presents the corresponding FTIR spectra, highlighting molecular rearrangements associated with carbonate decomposition, aluminosilicate reorganization and zeolite phase formation.

In the BHG_5-based systems, clear vibrational modifications can be observed in the carbonate region. Specifically, the ν_2 and ν_4 modes of calcite, at 872 and 713 cm^{-1} (Yu *et al.*, 1999; Joshi *et al.*, 2013), diminish or shift following alkaline activation (Fig. 7a–d). A sharper 872 cm^{-1} band and a shoulder at 866 cm^{-1} (García-Lodeiro *et al.*, 2010) appear in $GBHG_5{}^{550}$ specimens (Fig. 7b), with the shoulder remaining pronounced at 10 M NaOH, despite a decrease in intensity. This is indicative of a partial calcite-to-pirssonite transformation. Additionally, new bands at 687–688 cm^{-1} emerge in materials activated with 12–14 M NaOH, corresponding to $\nu_4CO_3^{2-}$ vibrations in pirssonite and other hydrated carbonates (Adler & Kerr, 1963; Estep *et al.*, 1970), reflecting the progressive rearrangement of carbonate ions and their transformation into secondary mineral phases.

In contrast, BHG_2-derived geopolymers (Fig. 7e–h) exhibit less pronounced spectral changes in the carbonate region. A weak band at ~1456 cm^{-1} suggests limited carbonation during curing (Bernal *et al.*, 2011); however, the absence of new crystalline sodium carbonates in the XRD data confirms that this effect is primarily non-crystalline. Unlike BHG_5, which shows the clear formation of pirssonite and other double carbonates, BHG_2 fails to undergo comparable secondary carbonate crystallization, probably due to its lower initial Ca content and reduced reactivity. Quartz remains unaffected in both systems, with persistent Si–O–Si stretching bands observed at 778–797 and 694 cm^{-1} (Lee & Van Deventer, 2003; Kaufhold *et al.*, 2012).

The inert behaviour of BHG_2 under alkaline conditions leads to negligible spectral variation, confirming the lack of geopolymerization processes. A pivotal indicator of structural reorganization in both matrices is the shift of the asymmetric Si–O–T stretching vibration. In BHG_5 specimens, this band shifts from 1023 cm^{-1} in the calcined clay to 1018–1019 cm^{-1} in the activated products (Chandrasekhar & Pramada, 1999; Heller-Kallai & Lapides, 2007), indicating increased cross-linking and the formation of Q^4 silicate environments.

A similar shift is observed in BHG_2 specimens, where the band transitions from 1031 to 997 cm^{-1} in the $GBHG_2{}^{550}$ series (Fig. 7f), suggesting the dissolution of reactive phases and subsequent gel formation. However, this shift is more pronounced in sample BHG_5, implying more extensive aluminosilicate restructuring. The bands at 476 cm^{-1} are attributed to the in-plane bending of Si–O and Al–O linkages (Post & Borer, 2002; Gao *et al.*, 2013), originating from the reconstruction of the AlO_4 and SiO_4 tetrahedra that characterize the geopolymer structure (Soleimani *et al.*, 2012).

Only BHG_5-based systems show evidence of zeolitic phase formation *via* FTIR spectroscopy (Ozer & Soyer-Uzun, 2015). The $GBHG_5{}^{750}$ spectra (Fig. 7c) show multiple bands at 732, 707, 662 and 433 cm^{-1}, attributed to four- and six-membered ring structures and Si–O–Al bending modes characteristic of hydrosodalite (Fernández-Jiménez & Palomo, 2005; Rees *et al.*, 2008; Liew *et al.*, 2012; Tchakouté *et al.*, 2016; González-García *et al.*, 2017; Sore *et al.*, 2020). These bands vary with NaOH concentration, confirming that zeolite nucleation is dependent on activator molarity. In contrast, the BHG_2 spectra do not display comparable ring-structure markers, indicating either limited or a lack of crystallization of zeolitic phases despite similar activation conditions. Water incorporation is observed in both systems through the appearance of bands in the 1600–1650 cm^{-1} range, which correspond to the bending vibrations of H–OH groups (Maragkos *et al.*, 2009). These bands are more prominent in BHG_5, probably due to a more extensive formation of gel-phase networks that retain bound water molecules. This moisture-related signature aligns with the greater curing efficiency and geopolymer stability observed in the BHG_5 formulations.

In summary, the FTIR data (Fig. 7) reveal that BHG_5-based geopolymers undergo more pronounced structural reorganization, including carbonate transformation, tetrahedral network development and zeolite crystallization, than those derived from BHG_2. These differences stem from the distinct chemical compositions and reactivities of the precursor clays, as well as their specific responses to thermal treatment and alkaline activation.

Compressive strength

Compressive strength tests conducted after 28 days of curing revealed marked differences in mechanical performance between geopolymers synthesized from BHG_2 and BHG_5 clays under varying thermal and alkaline conditions (Table 5). These differences reflect the interplay between mineralogical composition, phase evolution and gel cohesion.

BHG_2-based formulations generally displayed low compressive strength values, ranging from 0.48 to 1.7 MPa, with the notable exception of $^{10}GBHG_2{}^{950}$, which reached 6.14 MPa. Hence, calcination at 950°C activated the illitic clay sufficiently to enable improved mechanical development under 10 M NaOH. The improved performance probably stems from illite dehydroxylation and the partial crystallization of reactive species, which improved binder cohesion.

However, increasing the alkaline concentration to 12 and 14 M caused the compressive strength values to decline to 1.08 and 0.34 MPa, respectively, probably due to excessive pore formation and insufficient structural densification (Khale & Chaudhary, 2007; Zuhua *et al.*, 2009), as is supported by SEM observations (Fig. 8b). The compressive strength of samples calcined at 550°C and 750°C did not exceed 0.96 MPa, indicating poor activation efficacy at intermediate temperatures, in accordance with the limited amorphization and mineral transformation observed *via* XRD.

In contrast, BHG_5-based geopolymers developed substantially higher compressive strengths, ranging from 0.81 to 8.12 MPa, confirming that calcination at 750°C and activation with 12 M NaOH are the optimal conditions for developing mechanical strength. Comparable compressive strength levels have been reported in the literature for geopolymers based on illitic raw materials. For instance, Vasic *et al.* (2022) reported relatively low compressive strengths, not exceeding 13.7 MPa, for a geopolymer produced from a mixture of 40% low-illitic raw clay and 60% brick tile residue activated with 10 M KOH and Na_2SiO_3. Similarly, Seiffarth *et al.* (2013) obtained promising bending tensile strength values of ~8 MPa using a 50/50 feldspar/calcined clay mixture. The compressive strength improvement observed in the present study is primarily attributed to the decomposition of calcite during calcination (Figs 4e & 5b), which produces reactive CaO. This process

https://doi.org/10.1180/clm.2026.10034 Published online by Cambridge University Press

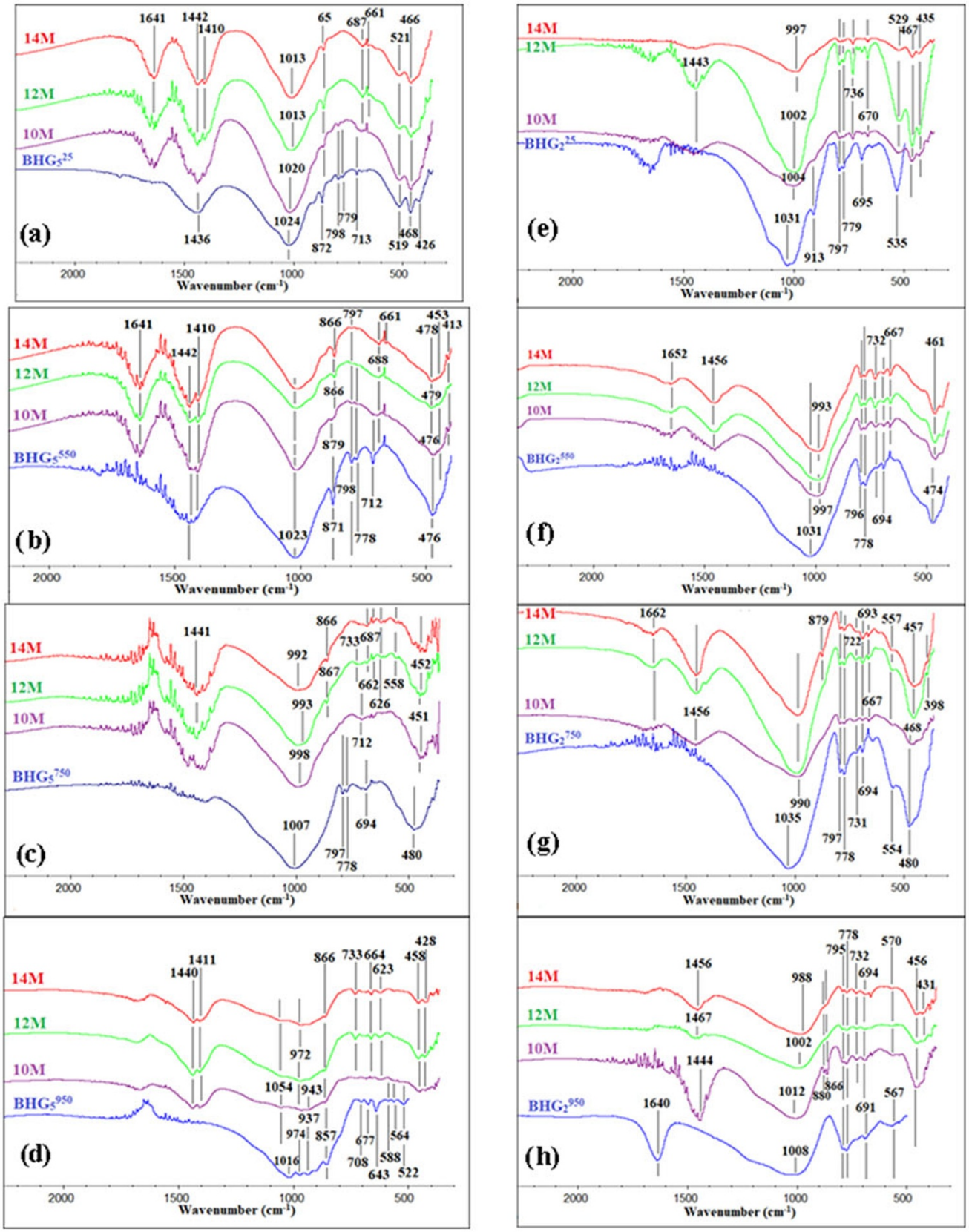

Figure 7. FTIR spectra (KBr pellet) of geopolymers synthesized from clay fractions (a–d) BHG_5 and (e–h) BHG_2. Precursors were calcinated at 25°C, 550°C, 750°C and 950°C and activated with 10, 12 and 14 M NaOH solutions.

https://doi.org/10.1180/clm.2026.10034 Published online by Cambridge University Press

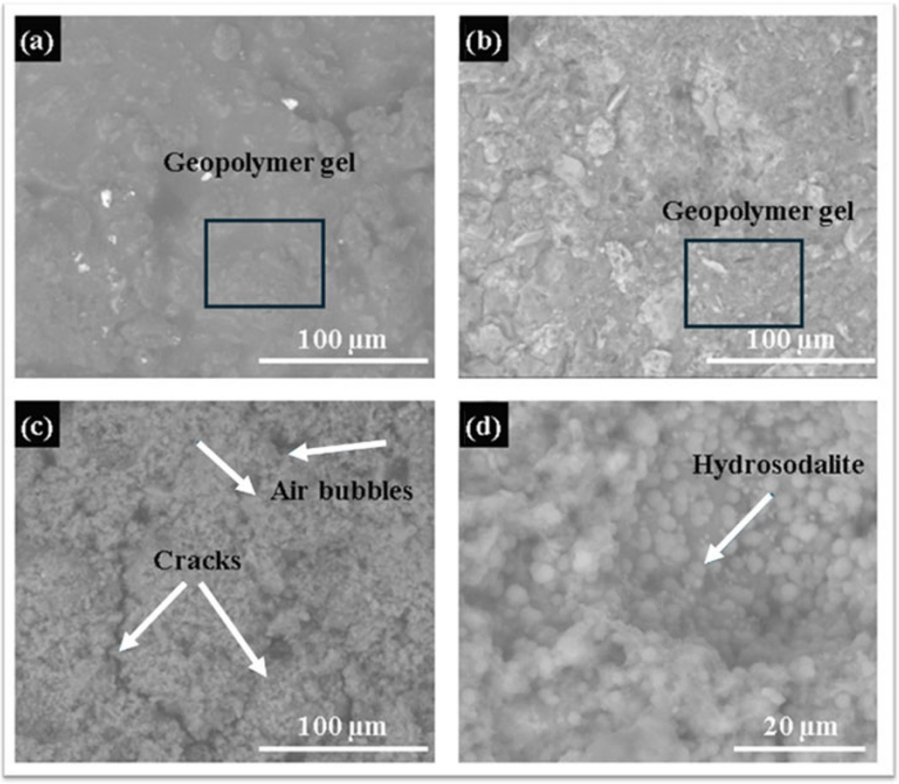

Figure 8. SEM micrographs of alkali-activated samples (a) $^{10}GBHG_2{}^{950}$, (b) $^{14}GBHG_2{}^{950}$, (c) $^{12}GBHG_5{}^{750}$ and (d) $^{12}GBHG_5{}^{750}$ at high magnification.

is clearly supported by the thermal analysis results, where BHG_5 exhibits a ∼2% weight loss at 700–800°C, consistent with calcite breakdown (Fig. 4e). Correspondingly, the calcite peak disappears in the XRD trace of BHG_5 after thermal treatment at 750°C (Fig. 5b), confirming the transition to CaO. Upon alkaline activation, the newly formed CaO reacts to generate secondary cementitious phases that improve matrix cohesion and contribute directly to the increased compressive strength observed in $^{12}GBHG_5{}^{750}$ (Prud'homme *et al.*, 2010, 2011; Essaidi *et al.*, 2013).

Specifically, CaO reacts with silicate species and Na^+ ions to form cementitious phases, which significantly promote gel densification and cohesion, thereby exceeding simple mechanical reinforcement. Other BHG_5 samples calcined at 750°C and activated with 10 or 14 M NaOH showed slightly lower, yet still substantial, compressive strengths of 6.64 and 4.32 MPa, respectively, indicating a robust activation window (Heah *et al.*, 2013). Samples calcined at 550°C ($GBHG_5{}^{550}$) yielded intermediate compressive strengths of between 4.32 and 6.54 MPa, highlighting effective reactivity due to metakaolinite formation and partial carbonate decomposition. Conversely, BHG_5 samples calcined at 950°C exhibited significant decreases in of compressive strengths (0.81–1.30 MPa). These decreases are attributed to the formation of inert crystalline phases, such as mullite and plagioclase (Mahmoudi *et al.*, 2010; Azzouz *et al.*, 2011), which reduced the available reactive content.

In summary, the BHG_5 clay demonstrates superior mechanical behaviour across various thermal and alkaline activation strategies. This is attributed not only to the aluminosilicate components but especially to its carbonate-rich composition, which generates reactive calcium oxide (CaO), leading to the nucleation of additional cementitious phases. In contrast, BHG_2, despite being richer in kaolinite, lacks this specific contribution and exhibits lower mechanical strength, except under specific high-temperature/low-alkalinity conditions. These findings underline the critical roles of precursor chemistry and thermal history in tailoring the mechanical properties of geopolymer binders.

Microstructural characteristics

Figure 8 presents the SEM micrographs of selected alkali-activated samples synthesized from BHG clays under various NaOH concentrations and calcination conditions. A comparison between $^{10}GBHG_2{}^{950}$ (Fig. 8a) and $^{14}GBHG_2{}^{950}$ (Fig. 8b) reveals notable microstructural differences despite the use of the same clay precursor (BHG_2 calcined at 950°C).

The $^{10}GBHG_2{}^{950}$ geopolymer exhibits a more homogeneous and slightly denser matrix compared to $^{14}GBHG_2{}^{950}$, which was synthesized using 14 M NaOH. The latter displays a more irregular and porous morphology, indicating a less efficient geopolymerization process. This suggests that excessive alkalinity may hinder the development of a cohesive matrix, consistent with the lower compressive strength observed for the 14 M NaOH-activated sample, which decreased from 6.34 to 0.34 MPa.

Figure 8c,d corresponds to the same sample, $^{12}GBHG5_{750}$. At a higher magnification (Fig. 8d), the formation of spherical particles becomes evident. These features are attributed to the crystallization of zeolitic phases, such as hydrosodalite (Felsche *et al.*, 1986; Vaičiukynienė *et al.*, 2016), as confirmed by XRD. Although the microstructure appears less compact compared to $^{10}GBHG_2{}^{950}$ and $^{14}GBHG_2{}^{950}$, sample $^{12}GBHG_5{}^{750}$ demonstrated the highest compressive strength (Table 5). This is attributed to the higher CaO content in the BHG_5 clay, which is ∼23.35 wt.% (Table 2).

https://doi.org/10.1180/clm.2026.10034 Published online by Cambridge University Press

Table 5. Compressive strength values (error ±0.05 MPa) of hardened geopolymer pastes synthesized from BHG_2 and BHG_5 clays calcined at various temperatures (550°C, 750°C and 950°C) and activated with various NaOH concentrations.

	$GBHG_2^{25}$				$GBHG_2^{550}$				$GBHG_2^{750}$				$GBHG_2^{950}$			
NaOH molar concentration	10	12	14	10	12	14	10	12	14	10	12	14	10	12	14	10
Compressive strength (MPa)	1.7	0.9	1.32	0.96	0.5	0.6	0.48	0.5	0.67	6.14	1.08	0.34	0.81	1.3	0.83	0.81
	$GBHG_5^{25}$				$GBHG_5^{550}$				$GBHG_5^{750}$				$GBHG_5^{950}$			
NaOH molar concentration	10	12	14	10	12	14	10	12	14	10	12	14	10	12	14	10
Compressive strength (MPa)	3	5.82	5.63	4.32	6.54	6.35	6.64	8.12	4.32	0.81	1.3	0.83	0.81	1.3	0.83	0.81

The high CaO content probably contributes to the formation of additional cementitious phases during activation (Bernal *et al.*, 2011). These CaO-rich phases increase structural densification and improve mechanical performance despite the apparent porosity (Bernal *et al.*, 2011).

Regarding the environmental stability and durability of the synthesized geopolymers, the materials developed, particularly from sample BHG_5, possess a stable matrix. The presence of calcite in the raw clay (BHG_5) leads to the formation of a hybrid geopolymeric network in which N–A–S–H and C–(A)–S–H gels coexist (Li & Ikeda, 2024; Stroscio *et al.*, 2024). This hybrid structure has been well documented to improve durability by reducing porosity and limiting the leaching of alkali ions (Garcia-Lodeiro *et al.*, 2011; Razeghi Tehrani *et al.*, 2024). Moreover, the formation of secondary crystalline phases such as hydrosodalite, observed in the XRD traces, contributes to the immobilization of the alkaline activator within the aluminosilicate framework. These microstructural features, combined with the significant compressive strength achieved (~8 MPa), indicate good potential for long-term stability in ambient conditions.

Conclusions

This study demonstrates the feasibility of synthesizing geopolymer binders from illitic-kaolinitic clays from southern Tunisia. The comparative analysis of BHG_2 and BHG_5 highlights that mineralogical impurities are pivotal to performance: the presence of carbonates in BHG_5 promotes the formation of secondary calcium-based cementitious phases after calcination at 750°C, leading to superior strength compared to the hematite-rich BHG_2.

The novelty of this work lies in the successful activation of low-purity illitic clays, shifting the focus from high-grade metakaolin to widely available regional resources.

The achieved compressive strength of ~8 MPa validates these binders for non-structural applications, such as stabilized earth blocks or interior partition units. Although the current mechanical results are moderate, they provide a solid baseline for the valorization of local Tunisian clays. Our future research will focus on further increasing this compressive strength to meet higher standards for other structural requirements and exploring the long-term durability of these binders under various environmental conditions. This study opens up a sustainable pathway for low-energy construction materials adapted to regional needs.

Supplementary material. The supplementary material for this article can be found at https://doi.org/10.1180/clm.2026.10034.

Author contributions. Conceptualization: ZJ, FG, IL, CL and SM; methodology: ZJ, CL and SM; software: ZJ and FG; validation: IL, CL and SM; formal analysis: ZJ; investigation: ZJ; resources: ZJ, FG, IL, CL, and SM; data curation: ZJ; writing – original draft preparation: ZJ; writing – review and editing: ZJ, FG, CL and SM; visualization: ZJ, FG, IL, CL and SM; supervision: CL and SM. All authors have read and agreed to the published version of the manuscript.

Acknowledgements. The authors are grateful to Dr Miriam Hanuskova, Department of Engineering 'Enzo Ferrari', University of Modena, and Reggio Emilia, Modena, Italy, for the BET surface area measurements.

Financial support. The authors are pleased to acknowledge the Tunisian Ministry of Higher Education and Scientific Research for its help in financing internships in Italy. The authors would also like to thank the University of Modena and Reggio Emilia (Italy) for covering the costs of materials and analyses.

Competing interests. The authors declare none.

References

Abdel-Gawwad H.A. & Abo-El-Enein S.A.A. (2016) Novel method to produce dry geopolymer cement powder. *HBRC Journal*, **12**, 13–24.

Adler H.H. & Kerr PF. (1963) Infrared spectra, symmetry and structure relations of some carbonate minerals. *American Mineralogist*, **48**, 839–853.

AFNOR. (1995) *Soils: Reconnaissance et essais, Détermination des limites d'Atterbeg – Limite de liquidité à la coupelle – Limite de plasticité au rouleau*. NF 94-051. Association Francaise de Normalisation, Paris, France, 15 pp.

AFNOR. (1998) *Soils: Investigation and Testing, Measuring of the Methylene Blue Adsorption Capacity of a Rocky Soil. Determination of the Methylene Blue Value of a Soil by Means of the Stain Test*. NF P 94-068. Association Francaise de Normalisation, Paris, France, 8 pp.

Allahverdi A. & Kani E.N. (2009) Construction wastes as raw materials for geopolymer binders. *International Journal of Civil Engineering*, **7**, 154–160.

Autef A., Joussein E., Gasgnier G., Pronier S., Sobrados I., Sanz J. & Rossignol S. (2013) Role of metakaolin dehydroxylation in geopolymer synthesis. *Powder Technology*, **250**, 33–39.

Azzouz H., Alouani R. & Tlig S. (2011) Mineralogical characterization of ceramic tiles prepared by a mixture of Cretaceous and Mio-Pliocene clays from Tunisia: factory and laboratory product. *Ceramic Society of Japan*, **119**, 93–100.

Baccour H., Medhioub M., Jamoussi F., Mhiri T. & Daoud A. (2008) Mineralogical evaluation and industrial applications of the Triassic clay deposits, southern Tunisia. *Material Characterization*, **59**, 1613–1622.

Barone G., Caggiani M.C., Coccato A., Finocchiaro C., Fugazzotto M., Lanzafame G. *et al.* (2020) Geopolymer production for conservation-restoration using Sicilian raw materials: feasibility studies. *IOP Conference Series: Materials Science and Engineering*, **777**, 012001.

Ben M'barek-Jemaï, M., Sdiri A., Ben Saad A., Boughalmi S., Ouerghi S., Themri M.R. & Chalouati Y. (2025) Geochemical characterization and ceramic properties of Aptian clays from Bargou–Bou Arada (north west of Tunisia). *Euro-Mediterranean Journal for Environmental Integration*, **10**, 5473–5487.

Ben Messaoud I., Hamdi N. & Srasra E. (2018a) Physico-chemical properties of geopolymer binders made from Tunisian clay. *Advances in Materials Science and Engineering*, **7**, 114–120.

Ben Messaoud I., Hamdi N. & Srasra E. (2018b) The suitability of thermally activated red illite/kaolinitic clay as raw material for geopolymer binders. *Material and Environmental Science*, **9**, 946–954.

Bernal S.A., Rodriguez E.D., Mejia de Gutiérrez R., Provis J.L. & Delvasto S. (2011) Activation of metakaolin/slag blends using alkaline solutions based on chemically modified silica fume and rice husk ash. *Waste and Biomass Valorization*, **3**, 99–108.

Boussen S., Sghaier D., Chaabani F., Jamoussi B. & Bennour A. (2016) Characteristics and industrial application of the Lower Cretaceous clay deposits (Bouhedma Formation), southeast Tunisia: potential use for the manufacturing of ceramic tiles and bricks. *Applied Clay Science*, **123**, 210–221.

Chalouati Y., Bennour A., Mannai F. & Srasra E. (2020) Characterization, thermal behaviour and firing properties of clay materials from Cap Bon Basin, north-east Tunisia, for ceramic applications. *Clay Minerals*, **55**, 351–365.

Chandrasekhar S. & Pramada P.N. (1999) Investigation on the synthesis of zeolite NaX from Kerala kaolin. *Journal of Porous Materials*, **6**, 283–297.

Chandrasekhar S. & Ramaswamy S. (2002) Influence of mineral impurities on the properties of kaolin and its thermally treated products. *Applied Clay Science*, **21**, 133–142.

Cong M., Bing C. & Longzhu C. (2016) Variables controlling strength development of self-compacting earth-based construction. *Construction and Building Materials*, **123**, 336–345.

Coulibaly B., Guillaume Pohan L.A., Kambiré O., Kouakou L.P.S., Goure-Doubi H., Diabaté D. & Ouattara L. (2020) Valorization of green clay from Bouaflé (Ivory Coast) in the simultaneous elimination of organic pollutants and metallic trace elements by adsorption: case of methylene blue and cadmium ions. *Chemical Science International Journal*, **29**, 37–51.

Csáki Š., Sunitrová I., Lukáč F., Łagód G. & Trník A. (2022) Thermal properties of illite-zeolite mixtures up to 1100 °C. *Materials*, **15**, 30–29.

D'Elia A., Pinto D., Eramo G., Giannossa L., Ventruti G. & Laviano R. (2018) Effects of processing on the mineralogy and solubility of carbonate-rich clays for alkaline activation purpose: mechanical, thermal activation in red/ox atmosphere and their combination. *Applied Clay Science*, **152**, 9–21.

Dathe F., Strelnikova V., Werling N., Emmerich K. & Dehn F. (2021) Influence of lime, calcium silicate and portlandite on alkali activation of calcined common clays. *Open Ceramics*, **7**, 100–152.

Davidovits J. (1991) Geopolymers: inorganic polymeric new materials. *Journal of Thermal Analysis and Calorimetry*, **37**, 1633–1656.

Davidovits J. (2002) 30 years of successes and failures in geopolymer applications. Market trends and potential breakthroughs. Presented at: *Geopolymer 2002 Conference*. Melbourne, Australia, 28–29 October.

Davidovits J. (2008) *Geopolymer Chemistry and Application*, 2nd edition. Institute Geopolymere, Saint-Quentin, France, 585 pp.

Dehmani Y., Bentahar I., Lgaz H., El-Kordy A., Aldalbahi A., Alrashdi A.A. *et al.* (2026) A critical review of natural clay minerals: structural characterization, textural properties, and adsorption mechanisms for sustainable wastewater treatment. *Materials Today Advances*, **29**, 100682.

Derouiche R., Zribi M. & Baklouti S. (2023) Study of carbonated clay-based phosphate geopolymer: effect of calcite and calcination temperature. *Minerals*, **13**, 284.

Duxson P., Provis J.L., Lukey G.C., Mallicoat S.W., Kriven W.M. & Van Deventer J.S.J. (2005) Understanding the relationship between geopolymer composition, microstructure and mechanical properties. *Colloids and Surfaces A: Physicochemical and Engineering Aspects*, **269**, 47–58.

Duxson P., Mallicoat S.W., Lukey G.C., Kriven W.M. & van Deventer J.S.J. (2007) The effect of alkali and Si/Al ratio on the development of mechanical properties of metakaolin-based geopolymers. *Colloids and Surfaces A: Physicochemical and Engineering Aspects*, **292**, 8–20.

El Boukili G., Lechheb M., Ouakarrouch M., Dekayir A., Kifani-Sahban F. & Khaldoun A. (2021) Mineralogical, physico-chemical and technological characterization of clay from Bensmim (Morocco): suitability for building application. *Construction and Building Materials*, **280**, 122300.

Elimbi A., Tchakoute H.K. & Njopwouo D. (2011) Effects of calcination temperature of kaolinite clays on the properties of geopolymer cements. *Construction and Building Materials*, **25**, 2805–2812.

Escalera E., Tegman R., Antti M.L. & Odén M. (2014) High temperature phase evolution of Bolivian kaolinitic-illitic clays heated to 1250 °C. *Applied Clay Science*, **101**, 100–105.

Essaidi N., Samet B., Baklouti S. & Rossignol S. (2013) Effect of calcination temperature of Tunisian clays on the properties of geopolymers. *Ceramics-Silikaty*, **57**, 251–257.

Essaidi N., Samet B., Baklouti S. & Rossignol S. (2014a) Feasibility of producing geopolymers from two different Tunisian clays before and after calcination at various temperatures. *Applied Clay Science*, **88–89**, 221–227.

Essaidi N., Samet B., Baklouti S. & Rossignol S. (2014b) The role of hematite in aluminosilicate gels based on metakaolin. *Ceramics-Silikaty*, **58**, 1–11.

Estep P.A., Kovach J.J., Hiser A.L. & Karr C.J. (1970) Characterization of carbonate minerals from oil shales and coals by infrared spectroscopy. Pp. 228–247 in: *Spectrometry of Fuels* (R.A. Friedel, editor). Plenum Press, New York, NY, USA.

Fabbri B., Gualtieri S. & Leonardi C. (2013) Modifications induced by the thermal treatment of kaolin and determination of reactivity of metakaolin. *Applied Clay Science*, **73**, 2–10.

Fernández-Jiménez A. & Palomo A. (2005) Mid-infrared spectroscopic studies of alkali-activated fly ash structure. *Microporous and Mesoporous Materials*, **86**, 207–214.

Ferone C., Liguori B. & Capasso I. (2015) Thermally treated clay sediments as geopolymer source material. *Applied Clay Science*, **107**, 195–204.

Foldvari M. (2011) *Handbook of Thermogravimetric System of Minerals and Its Use in Geological Practice*. Geological Institute of Hungary, Budapest, Hungary, 213 pp.

Gao K., Lin K. & Wang D. (2013) Effects of nano-SiO_2 on setting time and compressive strength of alkali activated metakaolin-based geopolymer. *The Open Civil Engineering Journal*, **7**, 84–92.

https://doi.org/10.1180/clm.2026.10034 Published online by Cambridge University Press

García-Lodeiro I., Fernández-Jiménez A., Palomo A. & Macphee D.E. (2010) Effect of calcium additions on N–A–S–H cementitious gels. *Journal of the American Ceramic Society*, **93**, 1934–1940.

Garcia-Lodeiro I., Palomo A., Fernández-Jiménez A. & Macphee D.E. (2011) Compatibility studies between N–A–S–H and C–A–S–H gels. Study in the ternary diagram Na_2O–CaO–Al_2O_3–SiO_2–H_2O. *Cement and Concrete Research*, **41**, 923–931.

Gharzouni A., Dupuy C., Sobrados I., Joussein E., Texier-Mandoki N., Bourbon X. & Rossignol S. (2017) The effect of furnace and flash heating on cox argillite for the synthesis of alkaliactivated binders. *Journal of Cleaner Production*, **156**, 670–678.

González-García D.M., Téllez-Jurado L., Jiménez-Álvarez F.J. & Balmori-Ramírez H. (2017) Structural study of geopolymers obtained from alkali-activated natural pozzolan feldspars. *Ceramics International*, **43**, 2606–2613.

Hajjaji M. (2014) Mineralogy and thermal transformation of clayey materials from the district of Marrakech, Morocco. *Geological Communication*, **101**, 75–80.

Hajjaji W., Moussi B., Hachani M., Medhioub M., Lopez-Galindo A., Rocha J.A. *et al.* (2010) The potential use of Tithonian–Barremian detrital deposits from central Tunisia as raw materials for ceramic tiles and pigments. *Applied Clay Science*, **48**, 552–560.

Hamdi N., Ben Messaoud I. & Srasra E. (2019) Production of geopolymer binders using clay minerals and industrial wastes. *Comptes Rendus Chimie*, **22**, 220–226.

Heah C.Y., Kamarudin H., Mustafa Al Bakri A.M., Bnhussain M., Luqman M., Khairul Nizar I. *et al.* (2013) Kaolin-based geopolymers with various NaOH concentrations. *International Journal of Minerals, Metallurgy, and Materials*, **20**, 313–322.

Hedfi I., Hamdi N., Srasra E. & Rodríguez M.A. (2014) The preparation of micro-porous membrane from a Tunisian kaolin. *Applied Clay Science*, **101**, 574–578.

Heller-Kallai L. & Lapides I. (2007) Reactions of kaolinites and metakaolinites with NaOH-comparison of different samples (part 1). *Applied Clay Science*, **35**, 99–107.

Hollanders S., Adriaens R., Skibsted J., Cizer Ö. & Elsen J. (2016) Pozzolanic reactivity of pure calcined clays. *Applied Clay Science*, **132–133**, 552–560.

Holtz R.D. & Kovacs W.D. (1981) *The Relationship between Geology and Landslide Hazards of Atchison, Kansas and Vicinity*. Kansas Geotechnical Survey, Current Research in Earth Science, Bulletin, part 3. Kansas Geological Survey, Lawrence, KS, USA, 244 pp.

Ilić B.R., Mitrović A.A. & Miličić L.R. (2010) Thermal treatment of kaolin clay to obtain metakaolin. *Hemijska Industrija*, **64**, 351–356.

Ionescu C., Simon V., Hoeck V. & Gál Á. (2025) Thermal behaviour of a carbonatic clay: a multi-analytical approach. *Minerals*, **15**, 390.

Ji J., Ge Y., Balsam W., Damuth J.E. & Chen J. (2009) Rapid identification of dolomite using a Fourier transform infrared spectrophotometer (FTIR): a fast method for identifying Heinrich events in IODP Site U1308. *Marine Geology*, **258**, 60–68.

Joshi S., Kalyanasundaram S. & Balasubramanian V. (2013) Quantitative analysis of sodium carbonate and sodium bicarbonate in solid mixtures using Fourier transform infrared spectroscopy (FT-IR). *Applied Spectroscopy*, **67**, 841–845.

Karunadasa K.S.P., Manoratne C.H., Pitawala H.M.T.G.A. & Rajapakse R.M.G. (2019) Thermal decomposition of calcium carbonate (calcite polymorph) as examined by *in-situ* high-temperature X-ray powder diffraction. *Journal of Physics and Chemistry of Solids*, **134**, 21–28.

Kaufhold S., Hein M., Dohrmann R. & Ufer K. (2012) Quantification of the mineralogical composition of clays using FTIR spectroscopy. *Vibrational Spectroscopy*, **59**, 29–39.

Khale D. & Chaudhary R. (2007) Mechanism of geopolymerization and factors influencing its development: a review. *Journal of Materials Science*, **42**, 729–746.

Konan K.L., Sei J., Soro N.S., Oyetola S., Gaillard J.M., Bonnet J.P. & Kra G. (2006) Caractérisation de matériaux argileux du site d'Azaguié-Blida (Anyama, Cote d'Ivoire) et détermination des propriétés mécaniques de produits céramiques. *Journal de la Société Ouest Africaine de Chimie*, **21**, 35–43.

LCPC. (1987) *Limites d'Atterberg, limite de liquidité, limite de plasticité*. Méthode d'essai n°19. Laboratoire Central des Ponts et Chaussées, Paris, France, 26 pp.

Lecomte I., Liégeois M., Rulmont A., Cloots R. & Maseri F. (2003) Synthesis and characterization of new inorganic polymeric composites based on kaolin or white clay and on ground-granulated blast furnace slag. *Journal of Materials Research*, **18**, 2571–2579.

Lee W.K.W. & Van Deventer J.S.J. (2003) Use of infrared spectroscopy to study geopolymerization of heterogeneous amorphous aluminosilicates. *Langmuir*, **19**, 8726–8734.

Li Z. & Ikeda K. (2024) Compositions and microstructures of carbonated geopolymers with different precursors. *Materials*, **17**, 1491.

Liew Y.M., Kamarudin H., Bakri A.M.M.A., Luqman M., Nizar I.K., Ruzaidi C.M. & Heah C.Y. (2012) Processing and characterization of calcined kaolin cement powder. *Construction and Building Materials*, **30**, 794–802.

Louati S., Baklouti S. & Samet B. (2016) Geopolymers based on phosphoric acid and illito-kaolinitic clay. *Advances in Materials Science and Engineering*, **7**, 2359759.

Luzu B., Duc M., Djerbi A. & Gautron L. (2024) High performance illitic clay-based geopolymer: influence of thermal/mechanical activation on strength development. *Applied Clay Science*, **258**, 107445.

Mahmoudi S., Srasra E. & Zargouni F. (2010) Firing behaviour of the lower cretaceous clays of Tunisia. *Journal of African Earth Science*, **58**, 235–241.

Mahmoudi S., Bennour A., Meguebli A., Srasra E. & Zargouni F. (2016) Characterization and traditional ceramic application of clays from the Douiret region in south Tunisia. *Applied Clay Science*, **127**, 78–87.

Maragkos I., Giannopoulou I.P. & Panias D. (2009) Synthesis of ferronickel slag-based geopolymers. *Minerals Engineering*, **22**, 196–203.

Martínez-Martínez S., Pérez-Villarejo L., Garzón E., Sánchez-Soto P.J. (2023) Influence of firing temperature on the ceramic properties of illite-chlorite-calcitic clays. *Ceramics International*, **49**, 24541–24557.

Merabtene M., Kacimi L. & Clastres P. (2019) Elaboration of geopolymer binders from poor kaolin and dam sludge waste. *Heliyon*, **5**, e01938.

Mezni M., Hamzaoui A., Hamdi N. & Srasra E. (2011) Synthesis of zeolites from the low-grade Tunisian natural illite by two different methods. *Applied Clay Science*, **52**, 209–218.

Mintsaev M., Murtazaev S.A., Salamanova M., Bataev D., Saidumov M., Murtazaev I. & Fediuk R. (2022) Structural formation of alkali-activated materials based on thermally treated marl and Na_2SiO_3. *Materials*, **15**, 1–14.

Nagendra P., Ganesh A.V., Hema H.C., Samarth Urs M., Prakash Narasimha K.N. & Suresh Kumar B.V. (2022) The Casagrande method for determining the consistency of granitic soil. *Materials Today: Proceedings*, **62**, 5660–5664.

Ounissi C., Mahmoudi S., Valentini L., Bennour A., Garbin E., Artioli G. & Montacer M. (2020) Potential use of Kebilian clay reserves (southern Tunisia) for the production of geopolymer materials. *Clay Minerals*, **55**, 101–111.

Ozer I. & Soyer-Uzun S. (2015) Relations between the structural characteristics and compressive strength in metakaolin based geopolymers with different molar Si/Al ratios. *Ceramics International*, **41**, 10192–10198.

Polcowñuk Iriarte I.A., Mocciaro A., Rendtorff N.M. & Richard D. (2025) Dehydroxylation of kaolinite: evaluation of activation energy by thermogravimetric analysis and density functional theory insights. *Minerals*, **15**, 607.

Post J.L. & Borer L. (2002) Physical properties of selected illites, beidellites and mixed-layer illite-beidellites from southwestern Idaho, and their infrared spectra. *Applied Clay Science*, **22**, 77–91.

Prud'homme E., Michaud P., Joussein E., Peyratout C., Smith A., Arii-Clacens S. *et al.* (2010) Silica fume as porogent agent in geo-materials at low temperature. *Journal of the European Ceramic Society*, **30**, 1641–1648.

Prud'homme E., Michaud P., Joussein E., Peyratout C., Smith A. & Rossignol S. (2011) *In situ* inorganic foams prepared from various clays at low temperature. *Applied Clay Science*, **51**, 15–22.

Prud'homme E., Autef A., Essaidi N., Michaud P., Samet B., Joussein E. & Rossignol S. (2013) Defining existence domains in geopolymers through their physicochemical properties. *Applied Clay Science*, **73**, 26–34.

Pulidori E., Lluveras-Tenorio A., Carosi R., Bernazzani L., Duce C., Pagnotta S. *et al.* (2022) Building geopolymers for CuHe part I: thermal properties of

https://doi.org/10.1180/clm.2026.10034 Published online by Cambridge University Press

raw materials as precursors for geopolymers. *Journal of Thermal Analysis and Calorimetry*, **147**, 5323–5335.

Rat E., Martínez-Martínez S., Sánchez-Garrido J.A., Pérez-Villarejo L., Garzón E. & Sánchez-Soto P.J. (2022) Characterization, thermal and ceramic properties of clays from Alhabia (Almería, Spain). *Ceramics International*, **49**, 14814–14825.

Razeghi Tehrani P., Arjomand M., Behbahaninia A. & Kargari N. (2024) Compatibility studies of N–A–S–H and C–A–S–H gels in alkali-activated geopolymer mortar. *Iranian Journal of Chemistry and Chemical Engineering*, **43**, 3737–3747.

Rees C.A., Provis J.L., Lukey C.G. & Van Deventer J.S.J. (2008) The mechanism of geopolymer gel formation investigated through seeded nucleation. *Colloids and Surfaces A: Physicochemical and Engineering Aspects*, **318**, 97–105.

Reig F.B., Adelantado J.V.G. & Moreno M.C.M.M. (2002) FTIR quantitative analysis of calcium carbonate (calcite) and silica (quartz) mixtures using the constant ratio method. Application to geological samples. *Talanta*, **58**, 811–821.

Sdiri A., Higashi T., Hatta T., Jamoussi F. & Tase N. (2010) Mineralogical and spectroscopic characterization, and potential environmental use of limestone from the Abiod formation, Tunisia. *Environmental Earth Science*, **61**, 1275–1287.

Seiffarth T., Hohmann M., Posern K. & Kaps C. (2013) Effect of thermal pretreatment conditions of common clays on the performance of clay-based geopolymeric binders. *Applied Clay Science*, **73**, 35–41.

Soleimani M., Naghizadeh R., Mirhabibi R. & Golestanifard F. (2012) Effect of calcination temperature of the kaolin and molar Na_2O/SiO_2 activator ratio on physical and microstructural properties of metakaolin-based geopolymers. *Iranian Journal of Chemistry and Chemical Engineering*, **9**, 43.

Sore S.O., Messan A., Prud'Homme E., Escadeillas G. & Tsobnang F. (2020) Comparative study on geopolymer binders based on two alkaline solutions (NaOH and KOH). *Journal of Minerals and Materials Characterization and Engineering*, **8**, 407–420.

Souri A., Kazemi-Kamyab H., Snellings R., Naghizadeh R., Golestani-Fard F. & Scrivener K. (2015) Pozzolanic activity of mechanochemically and thermally activated kaolins in cement. *Cement and Concrete Research*, **77**, 47–59.

Stroscio A., Barone G., Fernandez-Jimenez A., Lancellotti I., Leonelli C. & Mazzoleni P. (2024) Sicilian clay sediments as precursor for alkali activated materials. *Applied Clay Science*, **253**, 107–350.

Sumajouw M. & Rangan B.V. (2006) *Low-Calcium Fly Ash-Based Geopolymer Concrete: Reinforced Beams and Columns*. Research Report GC 3. Curtin University of Technology, Perth, Australia, 97 pp.

Tchakoute Kouamo H., Rüscher C.H., Kong S. & Kamseu E. (2016) Geopolymer binders from metakaolin using sodium waterglass from waste glass and rice husk ash as alternative activators: a comparative study. *Construction and Building Materials*, **114**, 276–289.

Vaičiukynienė D., Vaitkevičius V., Rudžionis Ž., Vaičiukynas V., Navickas A.A. & Nizevičienė D. (2016) Blended cement systems with zeolitized silica fume. *Construction and building Materials*, **22**, 299–304.

Van Riessen A. & Chen-Tan N. (2013) Beneficiation of Collie fly ash for synthesis of geopolymer part 2 – geopolymers. *Fuel*, **111**, 829–835.

Vasic M.V., Terzic A., Radovanovic Z., Radojevic Z. & Warr L.N. (2022) Alkali-activated geopolymerization of a low illitic raw clay and waste brick mixture. An alternative to traditional ceramics. *Applied Clay Science*, **218**, 106410.

Wang S., Gainey L., Mackinnon I.D.R., Allen C., Gu Y. & Xi Y. (2023) Thermal behaviors of clay minerals as key components and additives for fired brick properties: a review. *Journal of Building Engineering*, **66**, 105–802.

Wu D. (2024) Interfacial characteristics and mechanical behavior of geopolymer stabilizers with clay mineral: a molecular dynamics study. *Applied Clay Science*, **250**, 107286.

Yamchelou M.T., Law D.W., Patnaikuni I. & Li J. (2020) Alkali activation of mechanically activated low-grade clay. *Journal of Sustainable Cement-Based Materials*, **10**, 272–288.

Yu P., Kirkpatrick R.J., Poe B., McMillan P.F. & Cong X. (1999) Structure of calcium silicate hydrate (C–S–H): near-, mid-, and far-infrared spectroscopy. *Journal of the American Ceramic Society*, **82**, 742–748.

Zerzouri M., Hamzaoui R., Ziyani L., Yahia A. & Alehyen S. (2025) Enhancing illitic-clay geopolymer production: a comparative study of conventional method and mechanosynthesized pre-geopolymer powder. *Applied Clay Science*, **267**, 107727.

Zhang X., Wang J., Wang L., Li Z., Wang R., Li H. *et al.* (2022) Effects of kaolinite and its thermal transformation on oxidation of heavy oil. *Applied Clay Science*, **223**, 106507.

Zhang Z., Wang H. & Provis J.L. (2012) Quantitative study of the reactivity of fly ash in geopolymerization by FTIR. *Journal of Sustainable Cement-Based Materials*, **1**, 154–166.

Zibouche F., Kerdjoudj H., DeLacaillerie J.B. & Van Damme H. (2009) Geopolymers from Algerian metakaolin: influence of secondary minerals. *Applied Clay Science*, **43**, 453–458.

Zibret L., Wisniewski W., Horvat B., Bozic M., Gregorc B. & Ducman V. (2023) Clay rich river sediments calcined into precursors for alkali activated materials. *Applied Clay Science*, **234**, 106848.

Zuhua Z., Xiao Y., Huajun Z. & Yue C. (2009) Role of water in the synthesis of calcined kaolin-based geopolymer. *Applied Clay Science*, **43**, 218–223.

https://doi.org/10.1180/clm.2026.10034 Published online by Cambridge University Press